Research Square

Preprints are preliminary reports that have not undergone peer review.
They should not be considered conclusive, used to inform clinical practice,
or referenced by the media as validated information.

Ultrafast and Deep Fluoride Elimination from Emerging Fluoride-Containing Wastewater Enabled by Hydrogen Bonding Clusters of Guanidinium Engineered Cellulose

Guang Yang

guangyang@ahau.edu.cn

Anhui Agricultural University

Hanchen Wei

Anhui Agricultural University

Feihu Bi

School of Life Sciences, Key Laboratory of Jiangxi Province for Functional Biology and Pollution Control in Red Soil Regions

Shijie Zhang

Anhui Agricultural University

Xiaoling Zeng

Anhui Agricultural University

Shiting Zhang

Jinggangshan University

Hui Zhang

Anhui Agricultural University

Tian Liu

Hefei University of Technology

Liming Yang

Nanchang Hangkong University https://orcid.org/0000-0002-0199-2297

Xubiao Luo

School of Life Science, Jinggangshan University https://orcid.org/0000-0002-3935-1268

Article

Keywords:

Posted Date: October 26th, 2026

DOI: https://doi.org/10.21203/rs.3.rs-11335827/v1

License: This work is licensed under a Creative Commons Attribution 4.0 International License.
Read Full License

Additional Declarations: There is **NO** Competing Interest.

Ultrafast and Deep Fluoride Elimination from Emerging Fluoride-Containing Wastewater Enabled by Hydrogen Bonding Clusters of Guanidinium Engineered Cellulose

Hanchen Wei, [a, b] Feihu Bi, [b], Shijie Zhang, [a] Xiaoling Zeng, [a] Shiting Zhang, [b] Hui Zhang, [a, b] Tian Liu, [c] Liming Yang, [*, b] Guang Yang [*, a] Xubiao Luo, [*, b]

[a] Department of Material Science and Engineering, School of Material and Chemistry, Anhui Agricultural University, Hefei, Anhui 230036, China

[b] School of Life Sciences, Key Laboratory of Jiangxi Province for Functional Biology and Pollution Control in Red Soil Regions, Jinggangshan University, Ji'an, 343009, P. P. R. China

[c] School of Resources and Environmental Engineering, Hefei University of Technology, Hefei, 230009, P.R. China

*Corresponding author

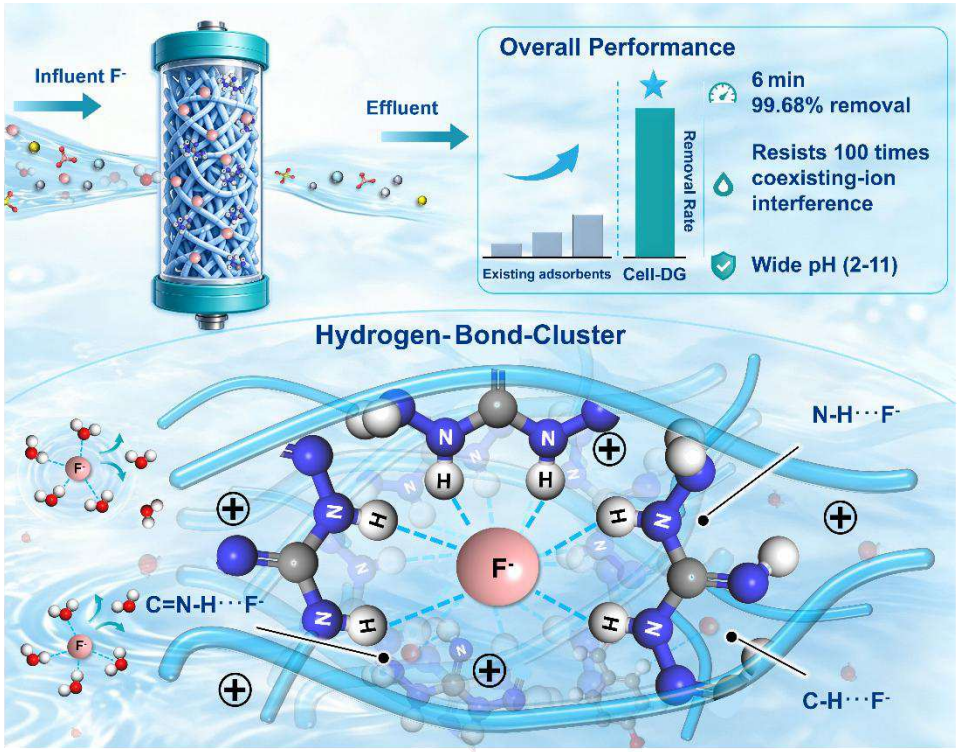
Tel.: +86 15026955892, 73183953371, 13576008526

E-mail: guangyang@ahau.edu.cn (G. Yang), luoxubiao@126.com (X. B. Luo), yangliming0809185@126.com (L. M. Yang)

ABSTRACT

The expansion of emerging industries generates substantial fluoride-bearing wastewater featuring harsh acid and alkali, and multiple interfering anions, making the deep removal of F^- remain a significant challenge. Herein, we report a guanidinium-engineered cellulose adsorbent that preorganized highly-dense constrained hydrogen-bond clusters (HBCs), enabling ultrafast and deep removal of fluoride from complex fluoride-bearing wastewaters. Guanidinium-engineered cellulose (Cell-DG) achieves a 99.68% fluoride removal within 6 min, over 100 times faster than reported metal-based and carbon/mineral-based fluoride adsorbents, while maintaining robust performance across a broad pH range of 2-11 and under a 100-fold excess of competing ions. Variable-temperature FTIR, ^{19}F NMR and critical control experiments support fluoride capture through N-H···F^- hydrogen bonds, with neighboring guanidinium donors converging around F^- forming high-density hydrogen-bonding clusters. Molecular dynamics simulations indicate partial hydration-shell rearrangement happens due to the competition of strong hydrogen bonding. Independent Gradient Model analysis further resolves cooperatively convergent guanidinium donors that stabilize F^- with a binding energy of up to -9.20 kcal mol^{-1}, much stronger than isolated C=N-H and C-H donors (-3.51 and -3.04 kcal mol^{-1}, respectively). In 6-day fixed-bed tests with simulated fluoride-bearing wastewaters, Cell-DG maintaining effluent fluoride concentrations below the drinking-water limit throughout, with a minimum of 0.09 mg L^{-1}. This work establishes HBCs recognition as a molecular design strategy for deep fluoride removal and recovery from complex low-concentration wastewaters.

Graphical abstract



Introduction

The accelerated expansion of emerging industries-spanning photovoltaics (PV), lithium-ion batteries (LIBs), semiconductors has become a vital linchpin for the global clean-energy transition and the advancement of artificial intelligence[1-4]. The whole manufacture and recycling processes of such emerging industries extensively rely on fluorinated chemicals and materials[5,6]. Unavoidably, the associated texturing, etching, cleaning, electrolyte-processing and material-purification steps generate substantial volumes of fluoride-bearing wastewater[7-10]. It is estimated that the annual output of fluorine-containing waste in China exceeds 50 million tons, with the total water consumption and wastewater discharge increasing by more than 10% annually[11]. Fluoride-bearing effluents remaining after primary treatment still contain residual fluoride at 8.0-37 mg L^{-1}, with pH values ranging from 2 to 11 and process-dependent coexisting ions (e.g., Cl^-, SO_4^{2-}, HCO_3^- and NO_3^-) at concentrations ranging from tens to over 10^3 mg L^{-1} (Table S1, Supporting Information). Certain industrial wastewater discharge standards permit fluoride concentrations of 8-10 mg L^{-1}, whereas the WHO drinking-water guideline is 1.5 mg L^{-1}, with a stricter limit of 1.0 mg L^{-1} in China (GB 5749-2022)[12-13]. These stringent thresholds help limit chronic excessive fluoride intake, which can cause dental and skeletal fluorosis, underscoring the importance of deep defluoridation[14]. This gap makes efficient and selective deep defluoridation from chemically complex, low-fluoride industrial wastewaters an urgent priority for safeguarding water resources and enabling sustainable development of emerging industry.

Current defluoridation routes fall into chemical precipitation, membrane separation, and adsorption[15-17]. Calcium-based precipitation and aluminum-based coagulation are established routes for fluoride removal. However, their application to deep defluoridation is constrained by CaF_2 solubility and slow precipitation kinetics in calcium-based systems, and by pH-dependent Al-F speciation and residual aluminum in aluminum-based systems[18-20]. Nanofiltration and reverse osmosis enable simultaneous fluoride and salt removal, although nanofiltration performance is sensitive to ionic strength and pH[21]. Adsorption including metal hydroxides, mineral phases, ion-exchange resins, carbonaceous supports, and functional polymers is particularly attractive for final polishing due to their structural stability, design flexibility, and ease of processing[22-25]. Fluoride adsorption mainly involves surface-hydroxyl exchange, M-F coordination, counter-anion exchange, and electrostatic or hydrogen-bonding interactions[26-29]. In metal-based sorbents, hydroxyl exchange and M-F coordination can be limited by pH-dependent site speciation and competition from strongly coordinating oxyanions. Conventional anion-exchange resins may preferentially retain competing anions over fluoride, whereas electrostatic capture at protonatable sites can weaken upon deprotonation. Separately, low fluoride concentrations can weaken concentration gradients and slow mass transfer, adding a kinetic constraint to these binding challenges[30]. These limitations highlight the need for adsorbents that combine high fluoride affinity and rapid uptake with tolerance to pH variations and complex competing ions at low fluoride concentrations.

The guanidinium group is a typical binding motif in the field of supramolecular

chemistry due to guanidyl groups exhibiting a strong affinity for anions through Y-shape matched hydrogen bonding[31,32]. Herein, we constructed a guanidinium-engineered cellulose adsorbent (Cell-DG) with preorganized high-density HBCs by grafting 1,3-diaminoguanidinium-derived units onto a cellulose scaffold, enabling deep fluoride removal from complex low-concentration wastewaters. The optimized Cell-DG exhibits a maximum fluoride uptake of 33.06 mg g^{-1}, reaches 99.7% of equilibrium uptake within 6 min, and maintains effective fluoride removal over a broad pH range and under a 100-fold excess of competing anions. Fixed-bed tests with simulated fluoride-bearing wastewaters further demonstrate deep fluoride polishing, followed by desorption and recovery of the captured fluoride. Combined experimental and computational analyses support cooperative fluoride capture through multiple hydrogen bonds within high-density hydrogen-bond clusters formed by neighboring guanidinium donors. This work establishes clustered hydrogen-bond recognition as a molecular design strategy for rapid and selective deep fluoride removal from complex low-concentration wastewaters, with potential applications in emerging industries.

Results

Synthesis and structural characterization of Guanidinium-Engineered Cellulose materials

Guanidinium-engineered cellulose adsorbents were synthesized by sequential chemical transformation of cellulose. Pristine cellulose was tosylated to T-Cell, followed by nucleophilic substitution with p-hydroxybenzaldehyde to yield Cell-DG_0, and final condensation with increasing DG feed to afford Cell-$DG_{0.5,\ 1,\ 2}$ (Fig. 1a,

Supplementary Fig. 1, 2, 3a). Solid-state nuclear magnetic resonance (ssNMR) spectroscopy and Fourier-transform infrared (FT-IR) spectroscopy collectively confirmed the incorporation of DG-derived guanidine moieties (Fig. 1b, c and Supplementary Fig. 3b). The aldehyde vibration at 1739 cm^{-1} disappeared after condensation, whereas a new N-H stretching band emerged at 3370 cm^{-1}. Corresponding cellulose- and guanidine-derived carbon resonances were observed between 60 and 160 ppm in the ssNMR spectra. Elemental analysis (EA) further showed that increasing the DG feed increased the nitrogen content from 3.991% to 5.497%, corresponding to DG mass fractions of 6.93-9.63% (Fig. 1d and Supplementary Table 2). Together, these results collectively support the construction of guanidine-enriched cellulose adsorbents with tunable grafting density.

Nitrogen adsorption-desorption isotherms exhibited type IV profiles with H_3-type hysteresis (Fig. 1e, f, Supplementary Table 3). Higher grafting densities expanded the BET surface area from 8.09 to 49.33 $m^2\ g^{-1}$and the BJH pore volume from 0.0450 to 0.0905 $cm^3\ g^{-1}$, while the primary pore size decreased from 3.68 to 2.63 nm. This textural evolution can be attributed to the heightened spatial exposure of guanidinium moieties along pore channels, improving the accessibility of N-H active sites. XRD and thermogravimetric analyses further characterized the structural changes accompanying modification (Supplementary Fig. 4, 5). SEM showed a wrinkled, irregularly porous (Supplementary Fig. 6), while the water contact angle decreased from 70.1° to 39.5° with increasing grafting degree (Supplementary Fig. 7), reflecting enhanced hydrophilicity that may enable to accelerate aqueous mass transport and improves site

accessibility during adsorption. The isoelectric point increased from 3.5 for Cell-DG_0 to 11.1 for Cell-DG_2, which retained a positive zeta potential at neutral pH (Supplementary Fig. 8). Variable-temperature FT-IR analysis revealed that, upon heating, the N-H stretching vibration of Cell-DG_2 blue-shifted from 3323.1 to 3343.8 cm^{-1}, while the C=N stretching vibration blue-shifted from 1649.5 to 1662.9 cm^{-1} (Fig. 1g and Supplementary Fig. 9). The blue shifts of these two bands, with essentially unchanged skeletal framework vibrations, indicates a thermally induced reconstruction of the N-H···N and N-H···O hydrogen-bonding network, confirming the presence of an ordered hydrogen-bonded cluster network.

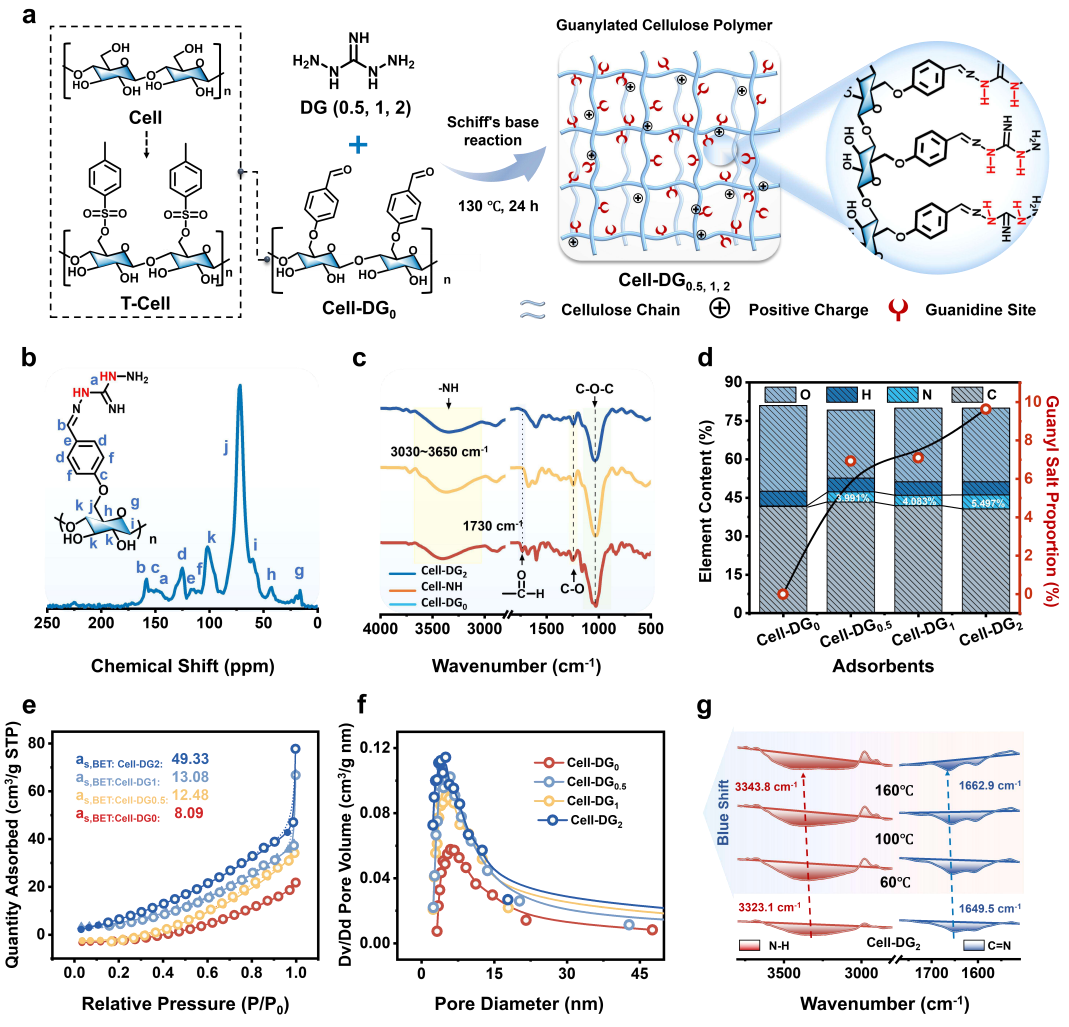


Fig. 1 | Construction and characterization of guanidinium engineered cellulose. a

Schematic illustration of the synthesis pathway for Cell-$DG_{0.5,\ 1,\ 2}$. **b** Solid-state NMR spectrum of Cell-DG_2. **c** FT-IR spectra of Cell-DG_0, Cell-NH, and Cell-DG_2. **d** Elemental composition and DG loading. **e** N_2 adsorption-desorption isotherms. **f** Pore size distribution diagram of Cell-$DG_{0,\ 0.5,\ 1,\ 2}$. **g** Variable-temperature FTIR spectra of the N-H and C=N bands.

Fluoride adsorption performance.

Adsorption performance evaluation revealed that Cell-DG exhibits a distinct dependence of F^- uptake on guanidine grafting density under equivalent fluorine content. Cell-DG_2 achieved a fitted Langmuir capacity of 33.06 mg g^{-1} at 25 °C, whereas Cell-DG_0 showed only limited uptake of 2.36 mg g^{-1} (Fig. 2a). The Langmuir model showed the Cell-DG_2 data is better than the Freundlich model (R^2 = 0.988 versus 0.897), consistent with saturation of a finite population of accessible sites (Supplementary Fig. 10 and Table 4). As shown in Fig. 2b, Cell-DG_2 reached a 99.68% of its equilibrium uptake within 6 min. The kinetic fits are provided in Supplementary Fig. 11, 12 and Table 5. This superior kinetic performance is attributed to the material's hierarchical porosity, which facilitates sustained F^- access to clustered guanidine sites[33-35]. Regeneration experiments using 0.1 M NaOH effectively restored the F^- adsorption capacity with a regeneration efficiency approaching 97.2-98.8% after six cycles (Fig. 2c). The slight capacity loss (<3%) indicates that 0.1 M NaOH can efficiently desorb F^- and regenerate the active sites. Temperature-dependent measurements gave negative ΔG values together with positive ΔH and ΔS values (Supplementary Fig. 13, Table 6, 7). Adsorption was thus favorable under the evaluated conditions and accompanied by

164 an entropy increase, consistent with solvent reorganization during binding. Capacity
165 alone, however, does not establish suitability for polishing dilute water. At an initial
166 fluoride concentration of 10 mg L^{-1}, Cell-DG_2 dosage of 0.6 g L^{-1} reduced the residual
167 concentration to 0.95 mg L^{-1} (Fig. 2d). Increasing the dosage to 1.5 g L^{-1} lowered it
168 further to 0.06 mg L^{-1}. The adsorption response therefore extended into the sub-mg L^{-1}
169 regime, where the treatment objective is a low final concentration rather than removal
170 of a large fluoride load.

171 The response to competing anions defined how far this polishing behaviour persisted
172 in chemically complex solutions. A test was performed in the presence of competing
173 anions. Cell-DG_2 maintained fluoride removal above 80% in the tested Cl^-, NO_3^-, SO_4^{2-}
174 , Br^-, I^-, phosphate, bicarbonate, and carbonate systems (Fig. 2e, Supplementary Fig.
175 14). Even at a 100-fold excess of competing ions, fluoride removal remained
176 approximately 80% (Fig. 2f). This resistance to ionic competition distinguishes Cell-
177 DG from adsorbents governed predominantly by nonspecific Coulombic attraction [36-
178 38]. Besides, Cell-DG_2 can retain more than 80% fluoride removal from pH 2 to 11, with
179 a maximum removal efficiency of 99.34% at pH 6 (Fig. 2g). The distribution ratios (α)
180 of HF and F^- species in solution at different pH values were calculated using Visual
181 MINTEQ 3.1 software. When pH < 3.18, fluorine primarily exists as HF; above pH
182 3.18, F^- gradually becomes the dominant species (Supplementary Fig. 15). A literature
183 comparison places Cell-DG among the fastest reported fluoride adsorbents while
184 retaining deep-removal capability (Fig. 2h, Supplementary Table 8). Collectively, these
185 results demonstrate that Cell-DG enables efficient F^- removal from low-concentration

wastewater with ultrafast kinetics, wide pH adaptability, and excellent anti-interference capability, establishing it as a robust platform for deep fluoride removal.

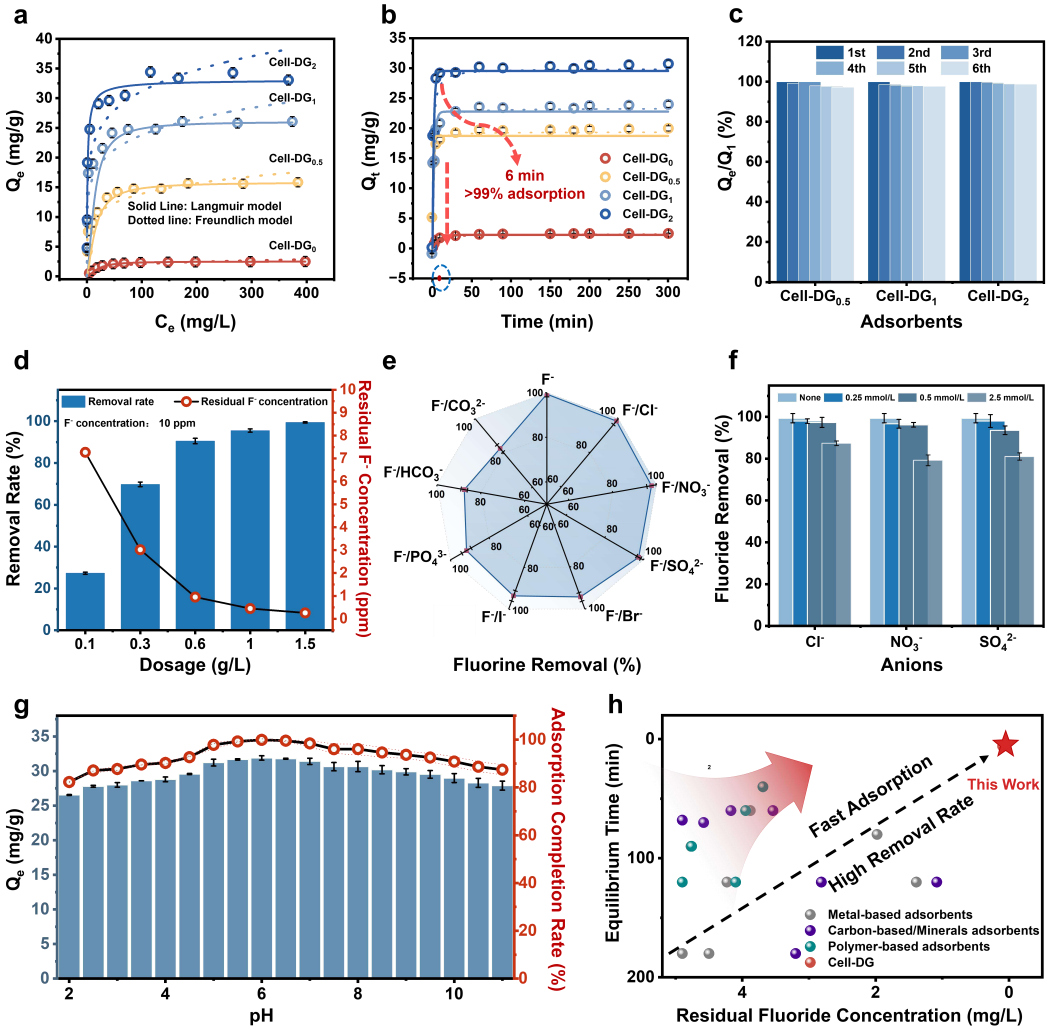


Fig. 2 | Rapid fluoride capture and coexisting-ion tolerance of Cell-DG adsorbents. **a** Adsorption isotherm data with Langmuir and Freundlich model fitting. **b** Kinetic adsorption curves with pseudo-first-order model fit. **c** Cyclic adsorption performance for F^- onto Cell-$DG_{0.5,\ 1,\ 2}$ (the eluent was 0.1 m NaOH; sorbent dosage was 1 g L^{-1}). **d** Fluoride removal performance and residual F^- concentration at an initial concentration of 10 ppm. **e** Fluoride removal in the presence of different competing anions. **f** Effects of increasing Cl^-, NO_3^- and SO_4^{2-} concentrations on fluoride removal. **g** Adsorption

capacity and removal efficiency of Cell-DG_2 across pH 2-11. **h** Comparison of uptake time and residual fluoride concentration with the selected literature adsorbents.

Mechanistic insights into divergence in fluoride recovery

The fundamental binding mechanism governing F^- adsorption onto guanidine-based polymer adsorbents was systematically elucidated through a combination of spectroscopic characterizations and computational modeling. Liquid-state ^{19}F NMR titration first established that the molecular precursor can associate with fluoride even in water. Incremental addition of NaF to 1,3-diaminoguanidine hydrochloride in D_2O induced a distinct up-field shift in the fluorine resonance, reaching a displacement of $\Delta\delta = 0.04$ ppm (Fig. 3a). The magnitude of this chemical shift progressively amplified and eventually stabilized at elevated F^- concentrations, directly signifying specific and saturable binding recognition between the guanidinium centers and F^-. Nonlinear curve fitting yielded an association constant (K_a) of 5.29×10^2 M^{-1} (corresponding to a dissociation constant, K_d, of 1.89×10^{-3} M), quantitatively confirming the formation of a host-guest complex. Fluoride uptake introduced an F 1s XPS signal at 684.9 eV and shifted the fitted N 1s components towards higher binding energies (Supplementary Fig. 16). The positive charge of Cell-DG_2 favours anion association, but does not by itself explain the observed fluoride affinity. To distinguish the effect of donor chemistry from surface charge, the amino-functionalized control Cell-NH was compared with Cell-DG_2. Although Cell-NH exhibited a comparable positive zeta potential to Cell-DG (approximately +36 mV), its fluoride-removal efficiency under a 0.5 mg L^{-1} initial concentration was only ≈20%, whereas Cell-DG achieved a remarkable removal

efficiency of 98.34% (Supplementary Fig. 17). This striking divergence suggests that while a cationic surface facilitates electrostatic pre-enrichment, pure electrostatic attraction is intrinsically insufficient for effective F^- capture. Urea, which specifically disrupts hydrogen bonds, and NaCl, which affects electrostatic interactions, were used for control analysis[39]. Increasing NaCl over 0-3 mg mL^{-1} caused a modest decrease in adsorption capacity, whereas urea produced a substantially larger loss (Fig. 3b, c, Supplementary Fig. 18). This sharp contrast demonstrates that directional hydrogen bonding serves as the primary interaction driving selective F^- recognition.

Spectroscopic analyses further pinpointed the specific molecular sites responsible for binding. In the concentration-dependent FTIR spectra (Fig. 3d, Supplementary Fig. 19), the N-H stretching vibration shifted toward higher wavenumbers from 3349 to 3378 cm^{-1} and eventually attenuated at a high F^- concentration (200 mg L^{-1}), owing to the modified energy barrier for N-H deformation upon F^- complexation. Simultaneously, the C=N stretching band displayed a distinct red shift from 1620 to 1608 cm^{-1}, indicating that the electron density of the conjugated guanidinium system was perturbed by F^-. Upon fluoride capture, the increased positive charge environment on the guanidinium group decreased the electron cloud density of the C=N bond, thereby lowering its vibrational frequency. To gain deeper thermodynamic insight into the driving force for F^- capture, variable-temperature FTIR (20 to 160 °C) was conducted to probe the thermal-sensitive of the hydrogen bonds (Fig. 3e, Supplementary Fig. 20). The N-H stretching maximum progressively shifted from 3327 to 3335 cm^{-1}, with a remarkably rapid shift occurring within the temperature window of 60 to 120 °C. This

thermal response is directly attributed to the weakening and disruption of the intermolecular N-H···F^- hydrogen bonds under elevated temperatures. To further investigate the interaction mechanism between F^- and Cell-DG, Density functional theory (DFT) calculations were performed. Geometry optimizations of the Cell-DG···F^- complex were carried out using the B3LYP-D3/6-31G(d)/SMD (water) method[40-45], which revealed that the complex adopts a donor-convergent binding geometry (Fig. 3f). To further understand the molecular recognition behavior, we calculated and mapped the molecular electrostatic potential (MEP) on the van der Waals surfaces of Cell-DG and F^-[47]. The optimized binding geometry is reasonable because molecules tend to approach each other in a manner that complements their electrostatic potentials. Moreover, comparative E_{bind} analyses consistently showed a preference for F^- across Cell-DG. Cell-DG exhibited the strongest F-Cell-DG E_{bind} of -6.25 eV, ≈1.1 to 1.9 times higher than those for competing ions (SO_4^{2-}, CO_3^{2-}, NO_3^-, Cl^-) (Fig 3f, g). The markedly stronger F^- binding over competing anions ensures that guanidine-rich sites preferentially capture F^- even in mixed-salt solutions, as reflected by the sustained adsorption capacity in our interference assays. This energetic hierarchy, governed by the local positive ESP, thus establishes Cell- DG as a robust sorbent for fluoride removal under complex ionic conditions.

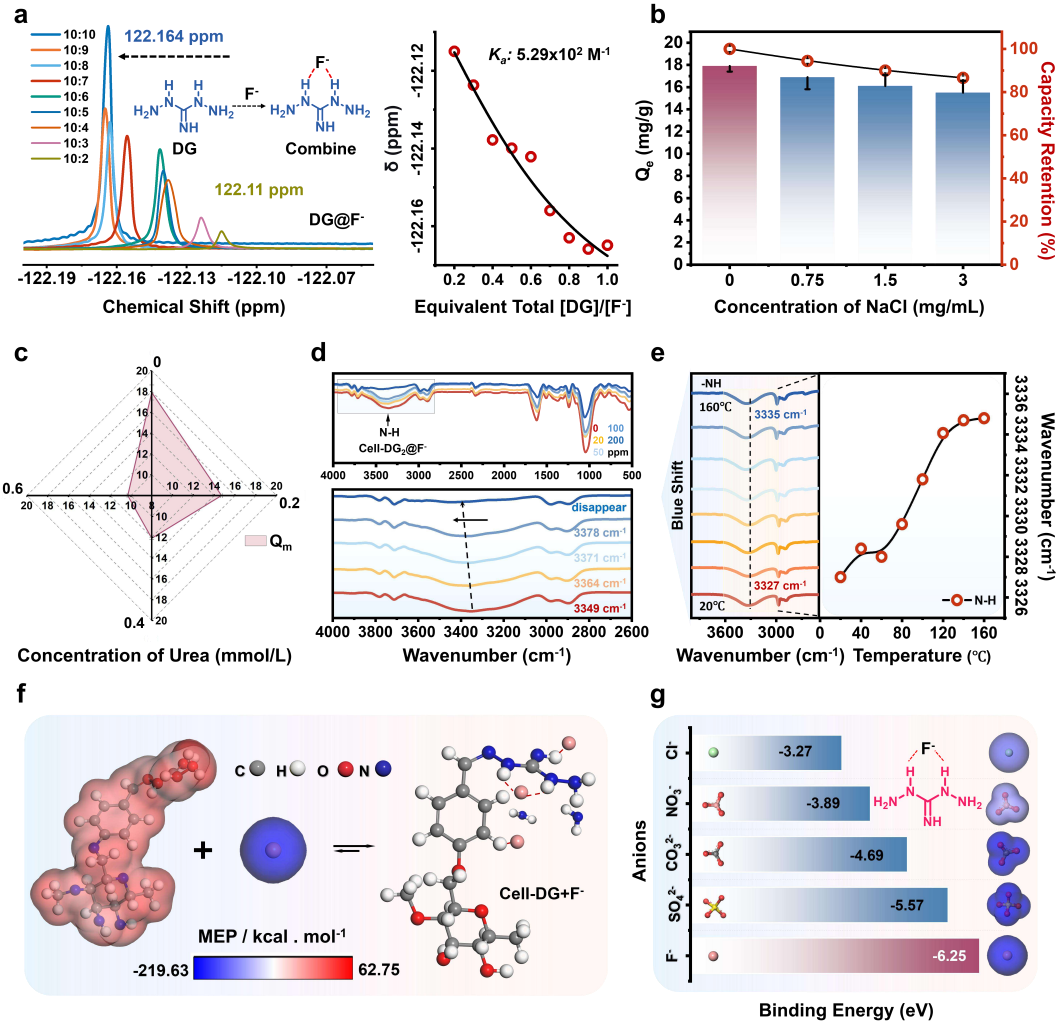


Fig. 3 | Evidence for hydrogen-bond-assisted guanidinium fluoride association. a ^{19}F NMR spectra at guanidine-to-fluoride molar ratios of 10:2 to 10:10, and fitting of the constant for the combination of guanidinium and fluoride ions. The influence of different concentrations of NaCl **b** and Ureal **c** on the adsorption capacity (Q_e) of F^- by Cell-DG_2. **d** FT-IR spectra and N-H stretching-band shifts of Cell-DG_2 at different fluoride adsorption concentrations. **e** The curve of the wavenumber of the N-H bond stretching vibration peak varying with temperature. **f** The optimized binding geometry of the Cell-DG·F^- complex (right) and the MEP-mapped molecular van der Waals surfaces of Cell-DG (left) and F^- (middle). **g** The Binding Energy of Cell-DG and

various anions.

Hydrogen-bond clusters (HBCs) capture coupled to hydration-shell rearrangement

Molecular dynamics (MD) simulations examined fluoride capture by neighboring guanidinium groups using the optimized Cell-DG polymer-chain model (Supplementary Fig. 21). As captured in the time-resolved simulation snapshots from 0 ns to 50 ns, F^- gradually transitions from a fully hydrated state in bulk aqueous solution to a localized, immobilized state firmly trapped by Cell-DG surface (Supplementary Fig. 22). This transition was accompanied by decreases in both the first-shell water coordination number and the number of $F^-\cdots H_2O$ hydrogen bonds (Fig. 4a and Supplementary Fig. 23), indicating partial rearrangement of the fluoride hydration shell upon interfacial binding. To elucidate how interfacial guanidine groups disrupt the intrinsic solvation shell of F^-, the spatial orientations and concentration profiles of interfacial H_2O molecules along the surface normal direction were quantitatively evaluated (Fig. 4b, c and Supplementary Fig. 24). For free F^- in pure water, the concentration distribution profile exhibits a distinct spatial phase separation: the primary density peak of H atoms (L_1) precedes that of O atoms (L_2) closest to the surface, with H peak intensity reaching nearly twice that of O (Fig. 4a). This structural feature signifies a highly ordered "H-down" interfacial water orientation, dictated by strong attraction between electron-rich $F\delta^-$ and $H\delta^+$ in H_2O. In sharp contrast, upon approaching the Cell-DG matrix (Cell-DG$\cdots F^-$), the L_1 and L_2 distribution peaks merge at virtually identical spatial positions with significantly broadened profile spans (Fig. 4b). This spectral convergence reveals a localized structural disorder of interfacial

water where “H-down” and “H-up” configurations dynamically coexist. The nature of host-guest H-bonding interactions governing F^- recognition was unraveled via radial distribution function (g(r)) analyses combined with site-specific geometric statistics (Fig. 4d, Supplementary Fig. 25). Structural calculations indicate that Cell-DG captures F^- by constructing a high-density hydrogen-bonding clusters network. Radial distribution function profiles plotted as a function of interatomic distance r display a prominent, sharp RDF peak centered at ~1.7 Å, demonstrating that the captured F^- is cooperatively stabilized by a spatially converging cluster of proximal guanidinium donors rather than a single isolated linkage. As schematically illustrated in Fig. 4e, the process begins with an encaged F^- anion shedding its ordered hydration shell as it approaches the adsorbent interface. Driven by competitive displacement by clustered N-H donors, the localized microenvironment evolves from an ordered, water-dominated hydration structure into a disordered, highly dehydrated state where F^- is tightly locked within a hydrogen-bonding network.

To further clarify the clustered hydrogen-bonding recognition mechanism between fluoride and the Cell-DG adsorbent, the hydrogen-donor centers were categorized into four distinct types: C=N-H (F176-H106), aromatic C-H (F179-H107), N-H (F177-H99, H104) and four donor *N-H clusters (F175-H56, H69, H64, and H61). By integrating Independent Gradient Model based on Hirshfeld partition (IGMH) and Reduced Density Gradient (RDG) analyses, the distinct types of hydrogen-bonding interactions exhibit clearly differentiated non-covalent features in three-dimensional space. The IGM iso-surface analysis explicitly illustrates (Fig. 4f) that robust N-H···F^- hydrogen

bonds are formed between the guanidinium groups of Cell-DG and F^- (dense blue iso-surfaces), whereas C-H···F^- interactions display only sparse green iso-surfaces. A pronounced hierarchical gradient in binding affinity toward fluoride ions is observed across the four hydrogen-donor types: guanyl *N-H (F175) delivers an average bond energy of -9.20 kcal mol^{-1} with H···F distances of 1.71-1.972 Å; guanyl N-H (F177) yields an average bond energy of -6.61 kcal mol^{-1} with H···F distances of 1.60-1.847 Å; while imine C=N-H (F176) and aromatic C-H (F179) exhibit substantially weaker average bond energies of only -3.51 and -3.04 kcal mol^{-1}, respectively. This hierarchy confirms that the guanidinium N-H group acts as the optimal proton donor for fluoride binding. Furthermore, IGM analysis on the Cell-NH···F^- complex (Supplementary Fig. 26) reveals markedly weak and localized green-to-cyan iso-surfaces, confirming the inferior donor capability of amino groups compared to guanidinium units. Quantitative topological parameters reveal that the positive Laplacian values ($\nabla^2\rho > 0$) across all bond critical points (BCPs) confirm the closed-shell nature of these interactions (Supplementary Fig. 27, Table 9). As the H···F distance contracts, the electron density $\rho(r)$ (0.01697 to 0.05725 a.u.), electron localization function (ELF), and localized orbital locator (LOL) values display strong positive correlations with the hydrogen-bond strength. Notably, when the hydrogen-bond energy strengthens beyond the threshold of -6 kcal mol^{-1}, the total energy density H(r) undergoes a sign reversal from positive to negative (e.g., H(r)=-0.01527 a.u. for F177-H99), marking a fundamental transition across the "covalency threshold" into a regime with pronounced partial covalent character. Combined experimental and theoretical results demonstrate that the

highly efficient capture of F^- by Cell-DG relies not on isolated single interactions, but on the synergistic effect of a high-density hydrogen-bonding cluster formed by multiple spatially adjacent guanidinium N-H donors with a single F^-. The emergence of partial covalent character provides the crucial thermodynamic driving force to overcome the high hydration energy of fluoride.

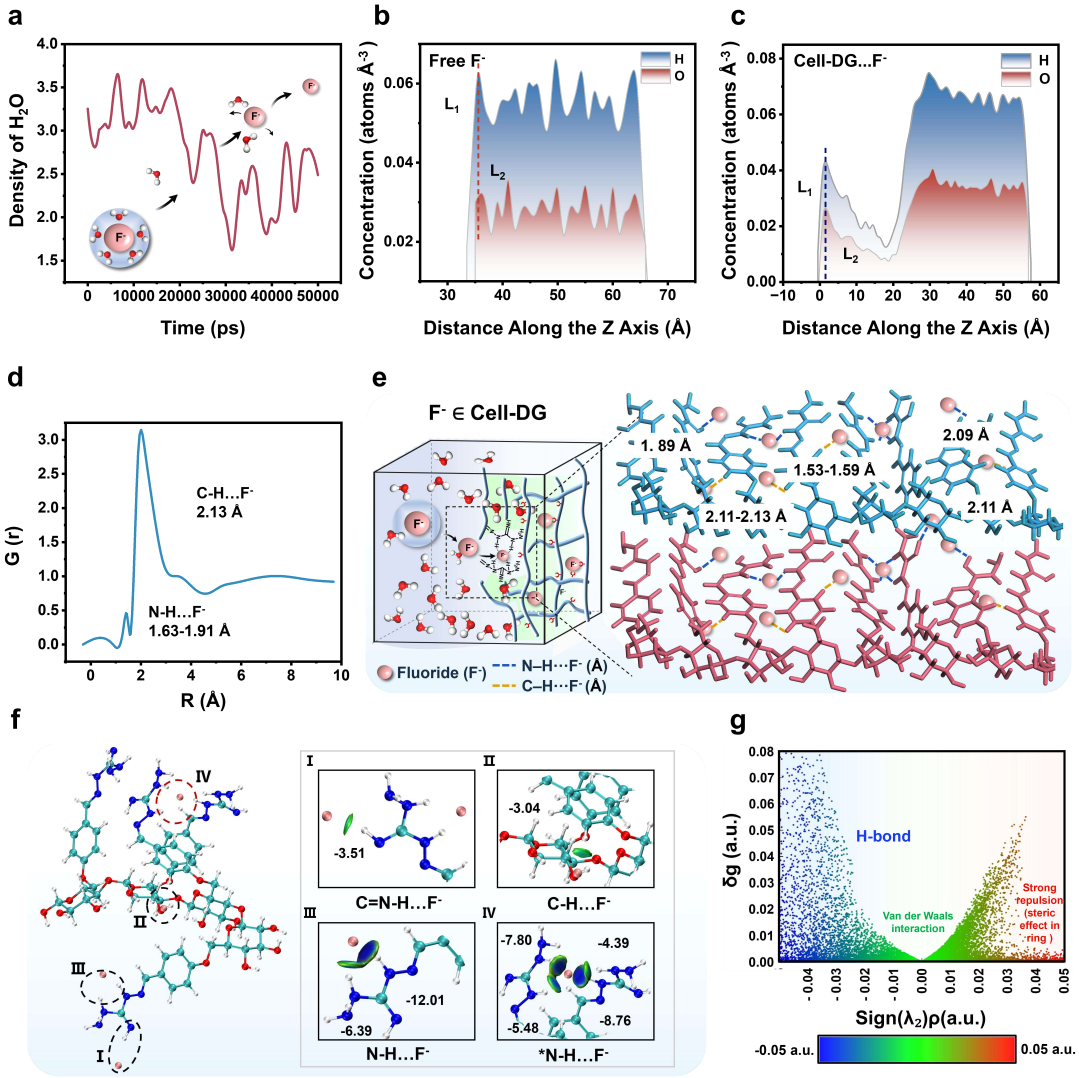


Fig. 4 | Hydrogen-bond-clusters binding geometry of Cell-DG and F^-. a The average number of water molecules within the first hydration layer before and after F^- adsorption. Distribution profiles of H and O concentrations along the surface normal direction on **b** free F^- and **c** Cell-DG···F^- represented the first density peak of H atoms closest to the

surface, while L_2 corresponded to the first density peak of O atoms. **d** The spherical atomic radial distribution function g plotted as a function of the interatomic distance *r* is shown. **e** Schematic illustration of the dehydration-driven fluoride capture process by Cell-DG. **f** Binding geometry of Cell-DG and F^-. IGM analyses and the distribution of non-covalent interactions in real space. (unit: kcal/mol) **g** δg^{inter}-0.01 a.u. isosurfaces colored by the sign of $(\lambda_2)\rho$ for the Cell-DG·F^- complex (the meaning of δg^{inter} and sign$(\lambda_2)\rho$ were in ref [47,48]). Blue indicates strong attraction, while red indicates strong repulsion.

Continuous-flow treatment, regeneration, and fluoride recovery

The variability of fluoride-bearing industrial waters highlights the need to assess continuous-flow performance in the presence of coexisting ions (Supplementary Table 10). We therefore evaluated Cell-DG_2 in fixed-bed columns using three simulated fluoride-bearing wastewaters (I-III), combining low fluoride concentrations with different coexisting-ion compositions (Fig. 5a, Supplementary Fig. 28). Before breakthrough, operation at 12 BV h^{-1} yielded effluent fluoride concentrations of 0.75, 0.66, and 0.09 mg L^{-1}, respectively (Fig. 5b). These concentrations correspond to approximately 95-99% fluoride removal, demonstrating effective capture from all three simulated wastewaters. Importantly, Cell-DG_2 combined sub-mg L^{-1} residual fluoride with dynamic adsorption capacities of 15.31-16.21 mg g^{-1}. These results extend the batch adsorption performance to continuous-flow treatment, showing that deep fluoride polishing can be sustained before breakthrough in different mixed-ion feeds. Cell-DG_2 also exhibited robust regenerability over 20 cycles, with markedly better performance

retention than the commercial adsorbent (Fig. 5c). Its cyclic efficiency decreased only slightly to approximately 96%, whereas that of the commercial adsorbent fell to approximately 79%. At cycle 20, Cell-DG_2 still provided an adsorption capacity of approximately 15 mg g^{-1}, more than twice that of the commercial adsorbent. The retained FT-IR bands and porous morphology after cycling further support preservation of its chemical framework and structure (Supplementary Fig. 29). The agreement between cyclic performance and structural characterization supports a regenerable fluoride-binding framework capable of repeated operation. Regeneration also enabled progressive fluoride enrichment, converting dilute fluoride capture into a resource-recovery opportunity. The fluoride concentration increased with the number of fixed beds, exceeding 2 g L^{-1} in the final eluate (Fig. 5d). The concentration contrast between the dilute feed and fluoride-rich eluate demonstrates that Cell-DG_2 can serve as a concentration medium as well as a polishing adsorbent. Subsequent $CaCl_2$ precipitation yielded crystalline CaF_2, as confirmed by XRD (Supplementary Fig. 30). This coupling of regenerable adsorption and mineral recovery channels the captured fluoride into a recoverable product instead of ending with a fluoride-loaded adsorbent.

To assess the economic implications of this combined treatment and recovery route, a preliminary techno-economic analysis was conducted using the assumptions in Supplementary Table 11. The modeled treatment cost was approximately ¥3.6 per tonne of wastewater (Supplementary Fig. 31a). Raw materials dominated the production cost at 96.31%, with LiCl and the DG precursor identified as important contributors (Supplementary Fig. 31b). This cost structure identifies reagent utilization and

389 synthesis optimization as priorities for improving process economics, complementing
390 the demonstrated benefit of repeated adsorbent reuse. Fig. 5e integrates these findings
391 into a process concept linking deep fluoride polishing, adsorbent regeneration, and CaF_2
392 recovery. In this configuration, the Cell-DG_2 fixed bed controls residual fluoride in
393 pretreated tailwater, while desorption concentrates the captured fluoride for subsequent
394 mineral recovery. The prospective industrial layout illustrates how this module could
395 be integrated downstream of existing pretreatment in the photovoltaic, semiconductor,
396 and lithium-ion battery industries. The combination of low residual fluoride, sustained
397 reusability, and recoverable fluoride concentrates provides a basis for advancing Cell-
398 DG_2 toward integrated tailwater treatment and resource recovery.

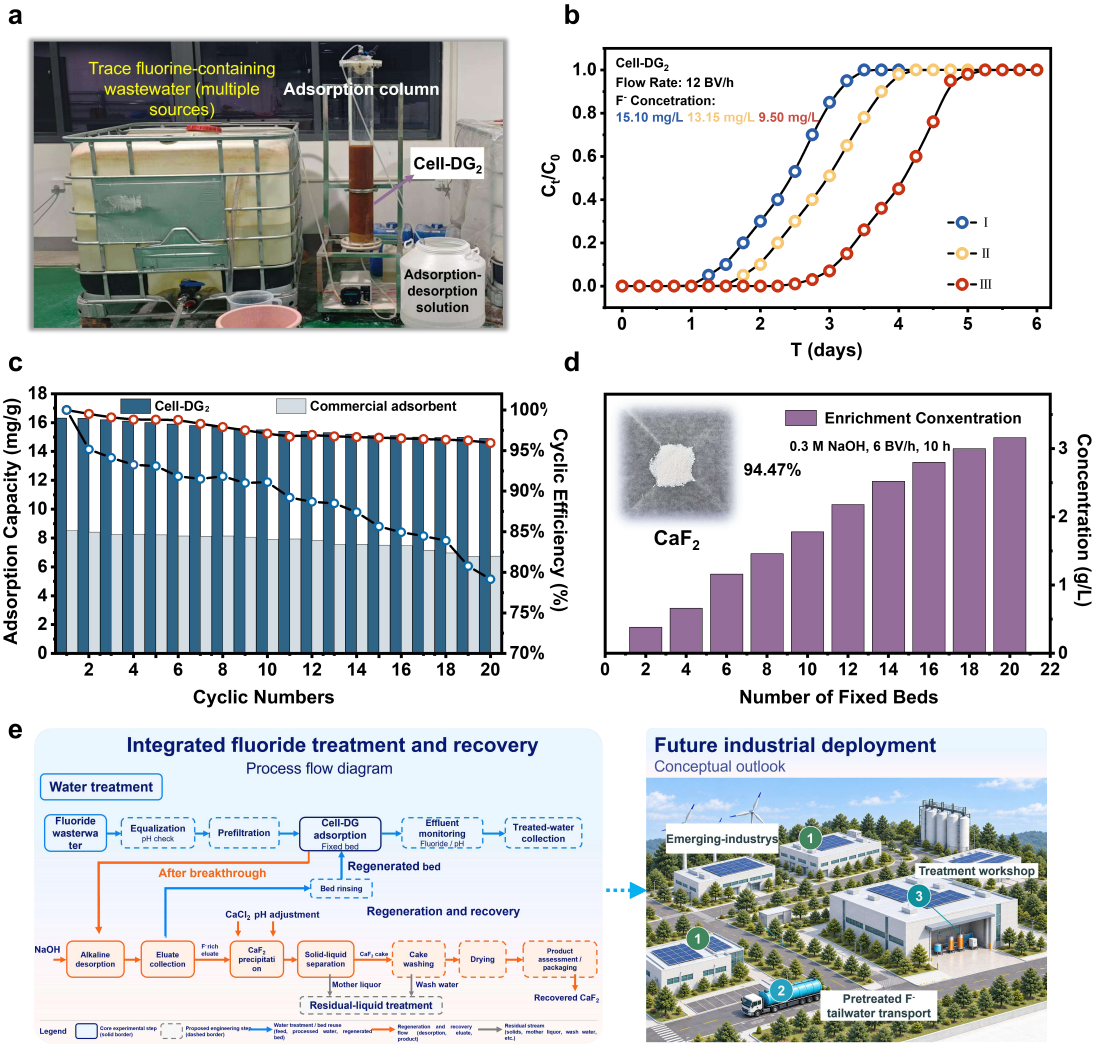


Fig. 5 | Continuous-flow fluoride removal, regeneration, and recovery. a Schematic diagram of the Cell-DG_2 adsorption column assembly. **b** Fluoride breakthrough curves after adsorption column treatment for simulated wastewaters I-III. **c** Recycling performance of Cell-DG_2 and commercial adsorbent. **d** Enrichment concentration of fluoride ions in the desorption solution after desorption by the adsorption column component. **e** Process concept integrating Cell-DG_2 adsorption, regeneration, and CaF_2 recovery (left), with prospective deployment in photovoltaic, semiconductor, and lithium-ion battery facilities (right).

Discussion

In summary, we developed a guanidinium-engineered cellulose adsorbent for ultrafast and deep fluoride removal from complex low-concentration wastewaters. Benefiting from the preorganized arrangement of neighboring guanidinium groups on the rigid cellulose scaffold, high-density hydrogen-bonding clusters were constructed to enhance fluoride recognition by facilitating interfacial enrichment, partial dehydration, and cooperative N-H···F^- binding. As a result, the optimized Cell-DG_2 reached 99.68% of its fluoride removal within 6 min and maintained efficient fluoride removal over a broad pH range of 2-11 and under a 100-fold excess of competing ions, demonstrating rapid adsorption kinetics and strong resistance to environmental interference. Six-day fixed-bed tests with simulated fluoride-bearing wastewaters demonstrated deep polishing before breakthrough, with effluent fluoride concentrations as low as 0.09 mg L^{-1}. The adsorbent also retained over 93% of its adsorption capacity after ten regeneration cycles. This work highlights preorganized high-density hydrogen-bond clusters as an effective molecular recognition strategy and provides new insight into the rational design of high-performance adsorbents for ultrafast and selective removal of trace anions from chemically complex wastewaters.

Methods

Full details of the methods are provided in the Supplementary Information (Supplementary Text S1-S9).

Data availability

The data supporting the findings of this study are available within the paper and its Supplementary Information files. Source data are available from the corresponding

authors upon request.

References

1. Rahdan, P., Zeyen, E. & Victoria, M. Strategic deployment of solar photovoltaics for achieving self-sufficiency in Europe throughout the energy transition. *Nat. Commun.* **16**, 6259 (2025).

2. Prince, K. J. et al. Sustainability pathways for perovskite photovoltaics. *Nat. Mater.* **24**, 22-33 (2025).

3. Wang, Y. et al. Fluorination in advanced battery design. *Nat. Rev. Mater.* **9**, 119-133 (2024).

4. Kang, J. H. et al. Monolithic 3D integration of 2D materials-based electronics towards ultimate edge computing solutions. *Nat. Mater.* **22**, 1470-1477 (2023).

5. Wang, Y. et al. Fluorine chemistry in rechargeable batteries: challenges, progress, and perspectives. *Chem. Rev.* **124**, 3494-3589 (2024).

6. Gao, X. et al. Research status of typical wastewater treatment technology for photovoltaic cell production process. *Chem. Eng. J.* **499**, 156523 (2024).

7. Wagner Wenz, R. et al. Removal and recovery of phosphorus and fluorine in process water from water based direct physical lithium-ion battery recycling. *Water Res.* **268**, 122476 (2025).

8. Qiu, Y. et al. Fast-selective electro-driven membrane reactor in fluoride/silica crystallization for microelectronic wastewaters recycling. *Water Res.* **282**, 123725 (2025).

9. Cao, S. et al. Fluoride-induced stress shapes partial denitrification granules to sustain microbial metabolism. *Water Res.* **275**, 123239 (2025).

10. Yin, Y. et al. Contact-electrocatalysis-electrocoagulation strategy with lithium-ion battery cathode. *Adv. Funct. Mater.* **36**, e77900 (2026).

11. Jhon, Y. I., Kim, Y., Park, J., Kim, J. H., Lee, T., Seo, M. & Jhon, Y. M. Significant exciton brightening in monolayer tungsten disulfides via fluorination: n-type gas sensing semiconductors. *Adv. Funct. Mater.* **26**, 7551-7559 (2016).

12. World Health Organization. Guidelines for drinking-water quality: fourth edition incorporating the first and second addenda (World Health Organization, 2022).

13. State Administration for Market Regulation and Standardization Administration of China. Standards for drinking water quality (GB 5749-2022) (2022).

14. Meena, L. & Gupta, R. Skeletal fluorosis. *N. Engl. J. Med.* **385**, 1510 (2021).

15. Qiu, Y. et al. Recovery of fluoride-rich and silica-rich wastewaters as valuable resources: a resource capture ultrafiltration-bipolar membrane electrodialysis-based closed-loop process. *Environ. Sci. Technol.* **56**, 16221-16229 (2022).

16. Damtie, M. M. et al. Removal of fluoride in membrane-based water and wastewater treatment technologies: Performance review. *J. Environ. Manage.* **251**, 109524 (2019).

17. Zhang, Y. et al. Steering electron density of Zr sites using ligand effect in bio-beads for efficient defluoridation. *Adv. Funct. Mater.* **33**, 2213999 (2023).

18. Deng, Z., Xu, A., Wei, X., Zhang, X. & Pan, B. Formation of aluminum‑fluoride complexes compromises defluoridation efficiency of aluminum-based coagulation. *Environ. Sci. Technol.* **58**, 14918-14928 (2024).

19. Deng, Z., Xu, A., Zhang, X., Zhang, K. & Pan, B. Effects of chelators on fluoride removal by $AlCl_3$ and Al_{13} coagulation: performance and mechanism. *Environ. Sci.*

Technol. **59**, 3297-3308 (2025).

20. Yang, J. et al. Fluorine recovery from low-concentration fluorine wastewater by flow-electrode capacitive deionization and fluid bed crystallization (FCDI-FBC): preconcentration and high-quality fluorite pellets formation. *Water Res.* **275**, 123228 (2025).

21. Pan, Z. et al. Molecular manipulation of polyamide nanostructures reconciles the permeance-selectivity threshold for precise ion separation. *Nat. Commun.* **16**, 7171 (2025).

22. Bera, B., Saha Chowdhury, S., Sonawane, V. R. & De, S. High capacity aluminium substituted hydroxyapatite incorporated granular wood charcoal (Al-HApC) for fluoride removal from aqueous medium: batch and column study. *Chem. Eng. J.* **466**, 143264 (2023).

23. Tordi, P., Ridi, F., Samorì, P. & Bonini, M. Cation-alginate complexes and their hydrogels: a powerful toolkit for the development of next-generation sustainable functional materials. *Adv. Funct. Mater.* **35**, 2416390 (2025).

24. Liu, C. et al. Simultaneous removal of fluoride and nitrate from photovoltaic wastewater utilizing a bifunctional polymer-based nanocomposite encapsulating Ce-Fe bimetal oxyhydroxides. *Chem. Eng. J.* **496**, 153990 (2024).

25. Wang, Z., Wang, X. & Yang, Y. Pillararene-based supramolecular polymers for adsorption and separation. *Adv. Mater.* **36**, 2301721 (2024).

26. Shen, P., Zhang, X., Xu, H. & Pan, B. Substitution-leaching-deposition (SLD) processes drive reversible surface layer reconstruction of metal oxides for fluoride

499 adsorption. *Environ. Sci. Technol.* **59**, 3814-3825 (2025).
500 27. Lau, K. et al. Differentiating between acidic and basic surface hydroxyls on metal
501 oxides by fluoride substitution: a case study on blue TiO_2 from laser defect engineering.
502 *Angew. Chem. Int. Ed.* **62**, e202213968 (2023).
503 28. Zhao, Z., Mi, Y., Wang, S., Du, X. & Zhang, Q. The high pKa-guided defect
504 engineering: improving fluoride removal in actual scenarios by benzimidazole
505 modulated metal-organic frameworks. *Water Res.* **280**, 123510 (2025).
506 29. Nguyen, D. A., Nguyen, V. B. & Jang, A. Integrated adsorption using ultrahigh-
507 porosity magnesium oxide with multi-output predictive deep belief networks: a robust
508 approach for fluoride treatment. *Chem. Eng. J.* **484**, 149586 (2024).
509 30. Wang, A. et al. Advanced fluidized bed-ultrafiltration-reverse osmosis process for
510 near-complete fluorine recovery from photovoltaic fluoride-laden wastewater: system
511 parameters and mechanisms. *Water Res.* **283**, 123858 (2025).
512 31. Xu, C. et al. Fast single metal cation conduction in ion-water aggregated aqueous
513 battery electrolytes. *Nat. Commun.* **16**, 4574 (2025).
514 32. Meng, Q.-W. et al. Guanidinium-based covalent organic framework membrane for
515 single-acid recovery. *Sci. Adv.* **9**, eadh0207 (2023).
516 33. Fang, Z. et al. Significance of fluorine chain-driven active sites for enhanced
517 selective lithium recovery. *Adv. Funct. Mater.* **36**, e18476 (2026).
518 34. Hu, H. et al. Ultra-selective and capacious lithium extraction from geothermal
519 brines via β -diketone functionalized brush-shaped polymer. *Adv. Funct. Mater.* **35**,
520 e13012 (2025).

35. Cho, W. et al. Supramolecular engineering of amorphous porous polymers for rapid adsorption of micropollutants and solar-powered volatile organic compounds management. *Adv. Mater.* **34**, 2206982 (2022).

36. Kumar, R. et al. State-of-the-art of research progress on adsorptive removal of fluoride-contaminated water using biochar-based materials: practical feasibility through reusability and column transport studies. *Environ. Res.* **214**, 114043 (2022).

37. Xiong, S. et al. Recent advances in selective recognition of fluoride with macrocyclic receptors. *Coord. Chem. Rev.* **461**, 214480 (2022).

38. Jangid, N. K. et al. Removal of fluoride ions from water using MgO-based materials with special emphasis on MgO/PPy nanocomposites: a review. *J. Mol. Liq.* 399, 124473 (2024).

39. Kong, J., Shen, M., Wang, G., Zhang, W., Wen, H. & Xie, J. Effects of hydrogen bonding and electrostatic interactions on the formation of rice starch-Mesona chinensis polysaccharide gels. *Food Hydrocoll.* **156**, 110322 (2024).

40. Becke, A. D. Density-functional thermochemistry. III. The role of exact exchange. *J. Chem. Phys.* **98**, 5648-5652 (1993).

41. Stephens, P. J., Devlin, F. J., Chabalowski, C. F. & Frisch, M. J. Ab initio calculation of vibrational absorption and circular dichroism spectra using density functional force fields. *J. Phys. Chem.* **98**, 11623-11627 (1994).

42. Hehre, W. J., Ditchfield, R. & Pople, J. A. Self-consistent molecular orbital methods. XII. Further extensions of Gaussian-type basis sets for use in molecular orbital studies of organic molecules. *J. Chem. Phys.* **56**, 2257-2261 (1972).

543 43. Hariharan, P. C. & Pople, J. A. The influence of polarization functions on molecular
544 orbital hydrogenation energies. *Theor. Chim. Acta* **28**, 213-222 (1973).
545 44. Grimme, S., Antony, J., Ehrlich, S. & Krieg, H. A consistent and accurate ab initio
546 parametrization of density functional dispersion correction (DFT-D) for the 94 elements
547 H-Pu. *J. Chem. Phys.* **132,** 154104 (2010).
548 45. Marenich, A. V., Cramer, C. J. & Truhlar, D. G. Universal solvation model based
549 on solute electron density and on a continuum model of the solvent defined by the bulk
550 dielectric constant and atomic surface tensions. *J. Phys. Chem. B* **113**, 6378 – 6396
551 (2009).
552 46. Bonaccorsi, R., Scrocco, E. & Tomasi, J. Molecular SCF calculations for the ground
553 state of some three-membered ring molecules: $(CH_2)_3$, $(CH_2)_2NH$, $(CH_2)_2NH_2^+$, (CH_2)
554 $_2O$, $(CH_2)_2S$, $(CH)_2CH_2$ and N_2CH_2. *J. Chem. Phys.* **52**, 5270-5284 (1970).
555 47. Lefebvre, C. et al. Accurately extracting the signature of intermolecular interactions
556 present in the NCI plot of the reduced density gradient versus electron density. Phys.
557 *Chem. Chem. Phys.* **19**, 17928-17936 (2017).
558 48. Lu, T. & Chen, Q. Independent gradient model based on Hirshfeld partition: a new
559 method for visual study of interactions in chemical systems. *J. Comput. Chem.* **43**, 539-
560 555 (2022).
561

Acknowledgements

This study was financially supported by the National Key Research and Development Program of China (Nos. 2024YFC3909700 and 2023YFC3904800), the "Harmless and Resourceful Utilization Technologies for Characteristic Lithium Ores", Strategic Priority Research Program of the Chinese Academy of Sciences (No. XDC0230000), the National Outstanding Young Scientists Fund (No. 52125002), the National Science Foundation of China (Nos. 52554013, 22476073, 52570141 and U24A20194), the Key Project of Jiangxi Provincial Research and Development Program (Nos. 20261BCG330008 and 20243BBI91001), Anhui Provincial Key Science and Technology Innovation Program (No. 202523anull050011), Jiangxi Provincial Natural Science Foundation (Nos. 20253BAC280012, 20262BAC200445, 20262BEJ730210, 20262BEJ730277, 20262BAC290015, 20262BAC290024, 20262BAC290011 and 20262BAC290027), the Jiangsu Special Fund on Technology Innovation of Carbon Dioxide Peaking and Carbon Neutrality (No. BT2024011), China Postdoctoral Science Foundation (Nos. 2024M751282 and 2025T180353), "Thousand Talents Program" of Jiangxi Province (No. S2021GDQN2161), the Key Project of Ganzhou City Research and Development Program (No. 2023PGX17350) and Doctoral Research Project Launched at Jinggangshan University (Nos. JZB2424, JZB2605 and JZB2549).

Author contributions

G.Y. conceived the idea and directed the project. H.W. designed and carried out the experiments and data analysis. S.Z., X.Z, and S.Z. assisted with some experiments. G.Y., L.Y., T.L., F.B., H.Z., and X.L. provided theoretical guidance. All the authors discussed

the results and commented on the paper.

Competing interests

The authors declare no competing interests.

Additional information

Supplementary information. Details of the chemical reagents, analytical methods, and instruments; synthesis procedures of the guanidinium-functionalized cellulose adsorbents (Cell-$DG_{0.5,\ 1,\ 2}$) and amino-functionalized control material (Cell-NH); comprehensive characterizations of the cellulose derivatives, including ^{1}H NMR, FT-IR, EA, GPC, XRD, TGA, SEM, XPS, BET, Contact Angle, and Zeta potential analyses, batch adsorption experiments including isotherm, kinetic, pH-dependent, competitive ion, fluoride removal efficiency, and thermodynamic studies, density functional theory (DFT) calculations with independent gradient model (IGMH) analyses and molecular dynamics (MD) simulations; statistical analysis ($n \geq 3$, mean ± standard deviation); continuous-flow fixed-bed column tests, and techno-economic analysis.

Supplementary Files

This is a list of supplementary files associated with this preprint. Click to download.

- SupplementaryInformation.pdf